



Hydrothermal synthesis of NiCeO_x nanosheets and its application to the total oxidation of propane

Zong Hu, Song Qiu, Yang You, Yun Guo, Yanglong Guo, Li Wang, Wangcheng Zhan*, Guanzhong Lu*

Key Laboratory for Advanced Materials and Research Institute of Industrial Catalysis, School of Chemistry and Molecular Engineering, East China University of Science and Technology, Shanghai 200237, PR China

ARTICLE INFO

Keywords:

Nickel oxide
Ceria
Propane combustion
Synergistic effect

ABSTRACT

A series of NiCeO_x mixed metal oxide catalysts with various Ce/(Ce + Ni) ratios were prepared using hydrothermal methods. The NiCeO_x catalyst with a 4% Ce/(Ni + Ce) molar ratio (NiCeO_x-4) demonstrated excellent catalytic performance for propane oxidation. Furthermore, the preparation method strongly affected the morphology and surface structure of the NiCeO_x-4 catalyst as well as its catalytic activity for propane oxidation. The NiCeO_x-4 catalyst that was prepared with the hydrothermal method exhibited a better catalytic performance compared with catalysts that were prepared by the co-precipitation method, sol-gel method and physical mixing of pure NiO and CeO₂ powders. The results demonstrated that Ni-containing CeO₂ (NiCeO_x) nanoparticles were located on the surface of the NiCeO_x-4 catalyst that was prepared using the hydrothermal method. As a result, the NiCeO_x-4 catalyst had strong reducibility, a large number of active oxygen species, and strong ability to break the C–H bond of propane, which led to higher catalytic activity for propane combustion.

1. Introduction

Volatile organic compounds (VOCs) are major air pollutants and can cause serious environmental pollution at low concentrations [1–4]. Hydrocarbons (HCs), one of the main components of VOCs, are mainly emitted from industrial processes or mobile sources and the quantity that is released in the atmosphere is continuously increasing. Light alkanes are the largest fraction of hydrocarbons (HCs) in automobile exhaust and their removal is difficult due to the stability of their molecular structure [5,6]. Since regulations that concern automotive emissions are becoming more stringent in many countries and the usage of liquefied petroleum gas (LPG), compressed natural gas (CNG) and liquefied natural gas (LNG) is increasing, the control of light alkane emission has attracted considerable attention and is currently one of the most urgent and compelling problems [7,8].

Catalytic combustion is an efficient route for VOC elimination because this method can efficiently convert pollutants completely into CO₂ and water. Supported noble metals, such as platinum and palladium, generally show good activity for the VOC combustion at relatively low temperatures [9–11]. However, in reality, their application is often limited by cost, high sintering rates or poisoning, especially by chlorinated compounds [12–16]. In contrast, low-cost transition metal oxides generally exhibit high thermal stability and poison resistance.

Therefore, transition metal oxide catalysts have been developed as a low-cost alternative to supported noble metals, especially for HC combustion. Recently, both DFT calculations and experimental results revealed that late transition metals such as Ni, Co, Cu are the main active compounds for breaking C–H and C–C bonds, which is a crucial step in the reaction process of HC steam reforming, oxidation and oxidative dehydrogenation [17–25].

Among the light alkanes from automobile exhaust emissions, the content of propane is the highest. At the same time, the molecular structure of propane is very stable, leading to the great difficulties in the activation of C–H bond and elimination of propane, which can well represent the characteristics in catalytic combustion of light alkanes [26]. Therefore, the total oxidation of propane is generally employed as a model reaction to assess the potential applications of the catalyst in the emission control of light alkane [7,27]. For propane combustion, the noble metal catalysts, such as supported Pt, Pd and Ru catalysts, generally possess the high catalytic activity [28–30]. Furthermore, the supports have great influence on the activity of the supported noble metal catalysts, among which zeolite is the preferred support to some degree [5,31,32]. On the other hand, many transition metal oxides have also been used for propane combustion, because of their low cost, high thermal stability and poison resistance mentioned above [7,33,34]. For example, NiO-based catalysts have been widely used in propane

* Corresponding authors.

E-mail addresses: zhanwc@ecust.edu.cn (W. Zhan), gzhlu@ecust.edu.cn (G. Lu).

combustion [33,35,36]. However, the activity of NiO-based catalysts for HC oxidation/combustion is typically lower than that of noble metals. Therefore, an enhancement in the catalytic performance of NiO-based catalysts for alkane combustion is increasingly important. The incorporation of ceria into nickel oxide is an efficient method because ceria presents high oxygen storage capability (OSC) and unique redox properties of $\text{Ce}^{4+}/\text{Ce}^{3+}$ redox pairs [37,38]. Moreover, the catalytic activities of NiO-based compound oxides can be tuned by controlling their structure and composition [39–41].

In this study, we prepared Ni-Ce-O mixed oxide catalysts and used propane as the model gas for light alkanes to evaluate their catalytic activity. The results demonstrated that the addition of a small amount of ceria can significantly enhance the catalytic performance of the nickel oxide catalyst and the preparation method of Ni-Ce-O mixed oxide catalysts markedly influenced their catalytic activity. Moreover, based on the characterization results of the catalysts, the relationships between the preparation method and the physicochemical and catalytic properties of Ni-Ce-O mixed oxide catalysts was disclosed.

2. Experimental section

2.1. Catalyst preparation

NiCeO_x nanosheets with Ce/(Ni + Ce) molar ratios that ranged from 0 to 10% (labelled from NiCeO_x-0 to NiCeO_x-10) were prepared using the hydrothermal method. For a typical NiCeO_x-4 sample, 0.576 mmol of $\text{Ni}(\text{NO}_3)_2 \cdot 6\text{H}_2\text{O}$ and 0.024 mmol of $\text{Ce}(\text{NO}_3)_3 \cdot 6\text{H}_2\text{O}$ were dissolved in 60 mL of deionized water, and 1.2 mmol of NaOH were dissolved in 20 mL of deionized water. Then, the two solutions were mixed together, stirred for 30 min at room temperature and transferred into a 100 mL Teflon-lined stainless steel autoclave. The autoclave was heated at 180 °C for 12 h and the obtained precursors were washed and centrifuged several times with deionized water. Finally, the products were dried at 100 °C overnight and then calcined at 400 °C in air for 1 h. Pure CeO₂ and NiO samples were prepared using the same procedures as those used for the NiCeO_x-4 sample.

For comparison, the NiCeO_x mixed oxide with a 4% Ce/(Ni + Ce) molar ratio was also prepared utilizing other methods. The NiCeO_x-CP sample was prepared with the co-precipitation method. Typically, 0.0576 mol of $\text{Ni}(\text{NO}_3)_2 \cdot 6\text{H}_2\text{O}$ and 0.0024 mol of $\text{Ce}(\text{NO}_3)_3 \cdot 6\text{H}_2\text{O}$ were dissolved in 50 mL deionized water. Then, 0.2 M NaOH solution was added dropwise to the mixed solution until pH = 10. After being stirred and aged at room temperature for 1 h, the solution was centrifuged and the obtained solid was washed several times with deionized water. The obtained precursor was dried at 100 °C overnight and then calcined at 400 °C in air for 1 h to obtain the product. The NiCeO_x-CA sample was prepared using the sol-gel method. Typically, 0.0576 mol of $\text{Ni}(\text{NO}_3)_2 \cdot 6\text{H}_2\text{O}$, 0.0024 mol of $\text{Ce}(\text{NO}_3)_3 \cdot 6\text{H}_2\text{O}$ and 0.072 mol of citric acid were dissolved in 50 mL of deionized water. Then, the solution was stirred at 80 °C for 2 h and the formed sol-gel was dried at 100 °C overnight. Finally, the obtained precursor was calcined at 400 °C in air for 1 h to obtain the product. The NiCeO_x-Mix sample was prepared by directly mixing pure NiO and CeO₂ powders that were prepared using the hydrothermal method.

2.2. Catalysts characterization

Powder X-ray diffraction (XRD) patterns of the catalysts were conducted on a Rigaku D/Max-RC diffractometer with Cu K α radiation ($\lambda = 1.5418 \text{ \AA}$) that was operated at 40 kV and 40 mA. The surface areas of the samples was measured on a Micromeritics ASAP 2400 instrument at 77 K and calculated using the Brunauer-Emmett-Teller (BET) method. The samples were degassed at 453 K for 12 h before the measurement. The transmission electron microscopy (TEM) was performed on a JEOL 2100F electron microscope that operated at 200 kV. HAADF-STEM and EELS elemental mapping images of the samples were

collected using a JEM-ARM200F spherical aberration-corrected electron microscope. The molar ratio of Ce/(Ni + Ce) in the samples was detected utilizing inductively coupled plasma-atomic emission spectroscopy (ICP-AES) on a Perkin-Elmer Optima 2100 DV spectrometer. X-ray photoelectron spectroscopy (XPS) spectra were obtained utilizing a VG ESCALAB MK II system that was equipped with a hemispherical electron energy analyser. The carbonaceous C 1s line (at 284.8 eV) was used as the reference to calibrate the binding energies. Raman spectra were recorded on a Renishaw Raman spectrometer under ambient conditions, and the 514 nm line of the Spectra Physics Ar⁺ laser was used as the excitation wavelength. The laser beam intensity and spectrum slit width was 2 mW and 3.5 cm^{-1} , respectively.

Temperature-programmed reduction (TPR), temperature-programmed surface reaction of propane (C_3H_8 -TPSR) and temperature-programmed desorption of O₂ (O₂-TPD) measurements of the catalysts were conducted using Micromeritics AutoChem II 2920 equipment. For H₂-TPR, a 50 mg sample was directly heated from room temperature to 800 °C at a rate of 10 °C/min in a flow of 10 vol.% H₂/Ar (40 mL/min). The hydrogen consumption was monitored using a thermal conductivity detector (TCD). For C_3H_8 -TPSR, a 50 mg sample was pretreated with 3 vol.% O₂/He at 400 °C for 30 min and then cooled to 50 °C. After being swept with 5 vol.% C_3H_8 /Ar for 1 h, the sample was heated from 50 to 500 °C at a rate of 10 °C/min in a flow of 5 vol.% C_3H_8 /Ar flow (40 mL/min). A mass spectrometer (HPR20 QIC) was used to monitor the effluent gas and the mass signals of CO₂ ($m/z = 44$) and propane ($m/z = 43$) were recorded. For O₂-TPD, a 50 mg sample was pretreated with 3 vol.% O₂/He (40 mL/min) at 400 °C for 30 min, then cooled to 50 °C and kept in 3 vol.% O₂/He (40 mL/min) for 1 h. After being purged with He for 1 h, the sample was heated from 50 to 500 °C at a rate of 10 °C/min in a flow of He (40 mL/min).

Diffuse reflectance infrared Fourier transform spectroscopy (DRIFTS) data were recorded on a Nicolet Nexus 670 FTIR spectrometer with 64 scans at an effective resolution of 4 cm^{-1} . Prior to the measurements, the sample was heated at 400 °C in Ar for 1 h and then cooled to 300 °C. After the background spectrum was recorded at 300 °C, Ar was replaced by the mixed gas (25 mL/min) of 0.5 vol.% C_3H_8 -5 vol.% O₂-94.5 vol.% Ar and *in situ* DRIFTS spectra of the samples were taken at a certain time. At the desorption stage, the mixed gas was switched to Ar (25 mL/min) and the DRIFTS spectra of the samples were again collected at a specific time.

2.3. Catalytic activity testing

The catalytic activity of the sample for propane oxidation was tested in a fixed-bed reactor that contained 200 mg of catalyst at atmospheric pressure. The feed gas consisted of 0.2 vol.% C_3H_8 + 2% vol.% O₂/Ar and its flow rate was 100 mL/min (GHSV = $30000 \text{ mL h}^{-1} \text{ g}^{-1}$). The heating rate is 2.5 °C/min. The conversion of C_3H_8 was measured after the catalytic reaction by an online gas chromatograph (GC-2060) that was equipped with an FID. The heating rate was 2 K/min. The C_3H_8 conversion ($X_{\text{C}_3\text{H}_8}$) was calculated using the following equation.

$$X_{\text{C}_3\text{H}_8} = \frac{[\text{C}_3\text{H}_8]_{\text{in}} - [\text{C}_3\text{H}_8]_{\text{out}}}{[\text{C}_3\text{H}_8]_{\text{in}}} \times 100\%$$

where $[\text{C}_3\text{H}_8]_{\text{in}}$ and $[\text{C}_3\text{H}_8]_{\text{out}}$ are the C_3H_8 concentrations in the inlet and outlet gas, respectively.

2.4. Kinetic measurements

The kinetic data for C_3H_8 oxidation was measured in a fixed-bed reactor at atmospheric pressure. The feed gas consisted of 0.2% $C_3H_8 + 2\%$ O_2/Ar (100 mL/min) and 50 mg of the catalyst that was diluted with 50 mg of inert quartz sand (40–60 mesh) was used for each test to remove both the internal and external diffusion. The propane conversion was controlled to be below 15%.

The reaction rate, $r_{C_3H_8}$ (mol/(g·s)), was calculated by the equation of $r_{C_3H_8} = X_{C_3H_8} V_{C_3H_8} / M$, where $X_{C_3H_8}$ is the conversion of C_3H_8 , $V_{C_3H_8}$ is the flow rate (mol/s) of C_3H_8 gas and M is the weight of the catalyst (g).

TOF (mol/(m² s)) was calculated with $TOF = X_{C_3H_8} V_{C_3H_8} / S$, where S is the surface area of the catalyst (m²).

2.5. Measurement of the reaction order

The reaction order of all the catalysts was measured in a fixed-bed reactor at atmospheric pressure. The feed gas consisted of $x\%$ $C_3H_8 + y\%$ O_2/Ar (100 mL/min) and 50 mg of the catalyst that was diluted with 50 mg of inert quartz sand (40–60 mesh) was used for each test to remove both the internal and external diffusion. The propane conversion was controlled to be below 15%.

The reaction order of all the catalysts was determined by the following equation [31]:

$$r = k(p_p^0)^\alpha (p_{O_2}^0)^\beta$$

where k is reaction constant, p_p^0 and $p_{O_2}^0$ are the partial pressures of propane and oxygen in the feed gas, respectively. α and β are the partial reaction order. During the determination of α value, the concentration of propane (x) in the feed gas was changed to obtain the different partial pressure of propane between 0.1 and 0.3 kPa, while the feed gas flow rate and the concentration of oxygen (y) in the feed gas was remained unchanged to obtain a fixed oxygen pressure ($p_{O_2}^0 = 2.0$ kPa). Similarly, during the determination of β value, the concentration of oxygen (y) in the feed gas was changed to obtain the different partial pressure of oxygen between 1.0 and 3.0 kPa, while the feed gas flow rate and the concentration of propane (x) in the feed gas was remained unchanged to obtain a fixed propane pressure ($p_p^0 = 0.2$ kPa).

3. Results and discussion

3.1. Catalytic activities of the NiCeO_x catalysts

Fig. 1A shows the catalytic activities of the NiCeO_x catalysts with varied Ce/(Ni + Ce) ratios during the total oxidation of propane. CO_2 and H_2O are the main products and no by-products were detected during the reaction, which indicates that propane was completely oxidized. The results indicate that pure CeO_2 exhibited a poor activity for

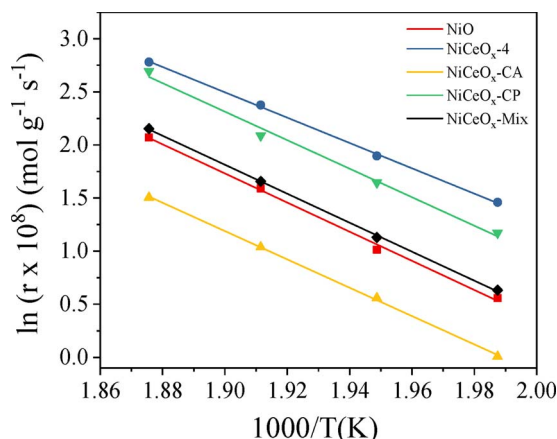


Fig. 2. Plots of $\ln r$ as a function of $1/T$ for NiO and NiCeO_x catalysts that were prepared with different methods. (The feed gas was 0.2% $C_3H_8 + 2\%$ O_2/Ar , and GHSV = 60000 h⁻¹).

the total oxidation of propane, whereas a high activity occurred with pure NiO. However, the incorporation of Ce into NiO can strongly enhance the catalytic activity of NiO. Amongst the NiCeO_x catalysts, NiCeO_x-4 showed the highest catalytic activity and T_{90} was at 300 °C, which is approximately 70 °C lower than that of pure NiO. Unfortunately, a further increase in the Ce/(Ni + Ce) molar ratio in the NiCeO_x catalysts to 7% and 10% would lead to the decrease in the catalytic activity of the NiCeO_x catalysts. Furthermore, the effect of the preparation method on the catalytic activity of the NiCeO_x catalysts for C_3H_8 oxidation was also investigated and the details are presented in Fig. 1B. The results demonstrate that the NiCeO_x-4 catalyst that was prepared using the hydrothermal method exhibits the highest catalytic activity and the catalytic activities follow the sequence: NiCeO_x-4 > NiCeO_x-CP > NiCeO_x-CA > NiCeO_x-Mix.

To compare the intrinsic catalytic activities of the NiCeO_x catalysts prepared with various methods, the Arrhenius plots of $\ln r$ versus $1/T$ for the NiCeO_x and pure NiO catalysts are depicted in Fig. 2. The reaction rate of each catalyst at 250 °C was calculated and is listed in Table 1. The reaction rate is 1.08×10^{-7} mol g⁻¹ s⁻¹ using the NiCeO_x-4 catalyst, which is higher than the rates of the pure NiO (4.90×10^{-8} mol g⁻¹ s⁻¹) and NiCeO_x catalysts that were prepared with other methods at the same temperature. The apparent activation energy (E_a) that was obtained from the slopes of the linear plots were also calculated. The results show that the incorporation of Ce into NiO can lower its E_a and the NiCeO_x-4 catalyst has the lowest E_a (99.1 kJ/mol) amongst all the catalysts. Moreover, the turnover frequency (TOF) of each sample was ranked in the order of NiCeO_x-4 (12.37 mol m⁻² s⁻¹) > NiCeO_x-CA (9.73) > NiCeO_x-CP (7.98) > NiCeO_x-Mix (6.72) > NiO (5.98), which further confirms that the addition of Ce can remarkably enhance the catalytic activity of NiO

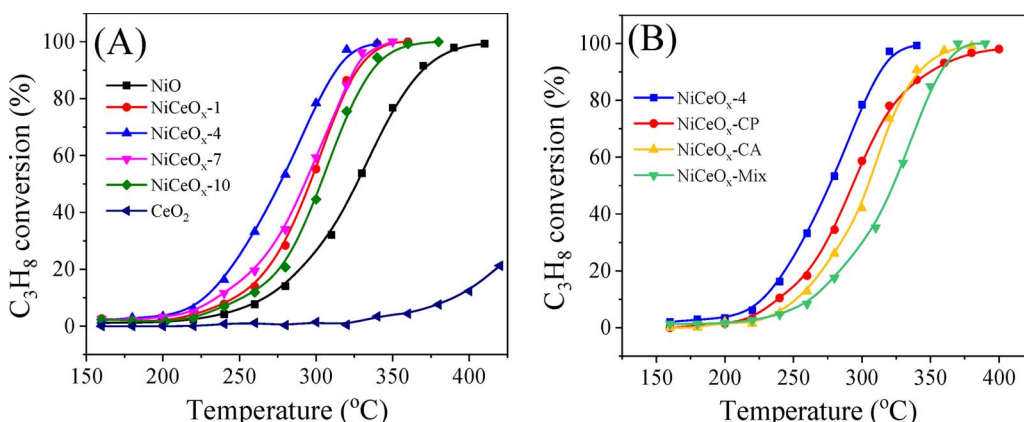


Fig. 1. The catalytic activities of NiCeO_x catalysts for propane oxidation. (A) NiCeO_x catalysts with various Ce/(Ni + Ce) molar ratios and (B) NiCeO_x catalysts that were prepared using various methods. (The feed gas was 0.2% $C_3H_8 + 2\%$ O_2/Ar , and GHSV = 30000 mL/g_{cat}h⁻¹).

Table 1
Catalytic performance of various results for NiO and NiCeO_x-4 samples.

catalyst	Ea (kJ/mol)	$r^a \times 10^8$ (mol g ⁻¹ s ⁻¹)	TOF ^a × 10 ¹⁰ (mol m ⁻² s ⁻¹)
NiO	114.0	4.90	5.98
NiCeO _x -4	99.1	10.76	12.37
NiCeO _x -CP	111.6	8.07	7.98
NiCeO _x -CA	110.9	2.82	9.73
NiCeO _x -Mix	113.4	5.24	6.72

^a The feed gas was 0.2% C₃H₈ + 2% O₂/Ar, and T = 250 °C.

and the hydrothermal route is an effective method to prepare the highly active NiCeO_x catalyst. On the other hand, the catalytic activity of the NiCeO_x-4 catalyst was compared with that of the catalysts reported in the references. As shown in Table 2, it can be found that the catalytic activity of the NiCeO_x-4 catalyst is much better than that of the catalysts reported in the references based on the TOF values.

To further determine the effect of Ce incorporation on the reaction kinetics over pure NiO, the reaction order for the NiO and NiCeO_x-4 catalysts was also studied and the corresponding results are presented in Fig. 3. All the partial order are slightly positive in both propane and oxygen and the reaction order is close to one. The reaction order of propane on the NiCeO_x-4 catalyst (0.42) was lower than that of the pure NiO (0.57), which indicates that the adsorption and activation of propane on the NiCeO_x-4 catalyst is stronger than that on NiO. Moreover, the reaction order with respect to O₂ on the NiCeO_x-4 (0.57) catalyst is close to that of NiO (0.58), which suggests that the incorporation of ceria has little influence on the sensitivity to the concentration of O₂.

To evaluate the potential application, the operation stabilities of the NiCeO_x-4 catalyst at 300 °C with and without H₂O was also measured at a GHSV of 30,000 mL h⁻¹ g_{cat}⁻¹ and the results are shown in Fig. 4. The results indicate that no marked deactivation appeared during the 40 h under normal reaction conditions (3–10 ppm vapour). When the content of H₂O in the reactant gas increased to 3 wt.%, the propane conversion over the NiCeO_x-4 catalyst also remained approximately constant (~75%) for 40 h, which indicates good water resistance. On the other hand, XRD (Fig. 5) and TEM (Fig. 6) results revealed that the structure and morphology of the NiCeO_x-4 catalyst were not changed after the stability test for 40 h without and with H₂O, confirming the high stability of the NiCeO_x-4 catalyst.

3.2. Catalyst characterization

3.2.1. XRD

The XRD patterns of the NiCeO_x catalysts are shown in Fig. 5. Only pure NiO displayed a rock salt structure (JCPDS 71-1179). As for the NiCeO_x catalysts, when the Ce/(Ni + Ce) molar ratio was lower than 7%, no diffraction peaks of CeO₂ were found, which indicates the high dispersion of CeO₂ in NiO. When the Ce/(Ni + Ce) molar ratio increased to 7%, the diffraction peaks corresponded to a typical cubic fluoride CeO₂ crystal phase (JCPDS 34-0394), which appeared in the patterns of the NiCeO_x catalysts. The values of NiO lattice parameters for each catalyst were calculated and no marked changes were found

(Table 3). In contrast, a slight difference was observed in the CeO₂ lattice parameters between the CeO₂ and NiCeO_x-10 catalysts. These results revealed a partial replacement of Ce⁴⁺ by Ni²⁺ in the framework of CeO₂ rather than the replacement of Ni²⁺ by Ce⁴⁺ in the framework of NiO, which is inconsistent with another report [42]. Alternatively, the XRD patterns of the NiCeO_x catalysts that were prepared with different methods are also shown in Fig. 5. Only the NiCeO_x-CA and NiCeO_x-CP catalysts exhibit the diffraction peaks of NiO, whereas the diffraction peak of CeO₂ at 28.5° is present in the XRD pattern of the NiCeO_x-Mix catalysts. Furthermore, the intensities of diffraction peaks of NiO for the NiCeO_x-CA, NiCeO_x-CP and NiCeO_x-Mix catalysts are weaker than that of the NiCeO_x-4 catalyst, which indicates that the crystallinity degree of the NiCeO_x-4 catalyst is higher compared with the NiCeO_x catalysts that were prepared by other methods.

3.2.2. TEM

TEM images of the NiO, CeO₂ and the NiCeO_x catalysts that were prepared with different methods are shown in Fig. 6. The pure NiO shows a hexagonal nanosheet morphology with an edge length of ~50 nm (Fig. 6A), whereas the pure CeO₂ catalyst that was prepared using the hydrothermal method exhibits polyhedrons with an edge length of ~10 nm (Fig. 6B). With the incorporation of Ce into pure NiO, the NiCeO_x-4 catalyst also exhibits a hexagonal nanosheet morphology, but its edge length of nanosheet decreased to ~30 nm (Fig. 6C). In contrary, when the Ce/(Ni + Ce) molar ratio increased to 7%, the morphology of the NiCeO_x-7 catalyst became irregular (Figs. 6D). As discussed above in the XRD results section, the diffraction peaks of the typical cubic fluoride CeO₂ crystal phase are present for the NiCeO_x-7 catalyst, which may cause a morphology change from hexagonal nanosheet to an irregular shape. Furthermore, the preparation method also influenced the morphology of the NiCeO_x catalysts. The NiCeO_x-CP catalyst is composed of many irregular polyhedrons with high-density stacking, whereas the NiCeO_x-CA catalyst exhibited a similar morphology with higher agglomeration, which led to a low BET surface area (shown in Table 3).

To further identify the structural details of the NiCeO_x-4 catalyst, HAADF-STEM and EELS elemental mapping images of the NiCeO_x-4 and NiCeO_x-Mix catalysts were collected and are shown in Fig. 7. These results demonstrate that CeO₂ tends to aggregate to the nanoparticles on both the NiCeO_x-4 and NiCeO_x-Mix catalysts. However, the size of CeO₂ nanoparticles on the NiCeO_x-4 catalyst (4–6 nm) is smaller than that on the NiCeO_x-Mix catalyst (15 nm), which is in agreement with the XRD results. Furthermore, the elemental compositions of the selected area (red triangle) in Fig. 7 for the NiCeO_x-4 and NiCeO_x-Mix catalysts are listed in Table 4. Interestingly, 9.47 wt.% of Ni is present in the selected signal CeO₂ nanoparticle on the surface of the NiCeO_x-4 catalyst, which indicates that a specific quantity of Ni was incorporated into CeO₂ to form NiCeO_x nanoparticles. This partial replacement of Ce⁴⁺ by Ni²⁺ in the framework of CeO₂ was also proposed in the XRD results. In contrast, elemental Ni was absent in the selected signal CeO₂ nanoparticle on the surface of the NiCeO_x-Mix catalyst. In summary, CeO₂ exists as NiCeO_x nanoparticles that are supported on the NiCeO_x-4 catalysts, whereas pure CeO₂ nanoparticles are supported on the NiCeO_x-Mix catalysts.

Table 2
Comparison of the catalytic results of NiCeO_x-4 catalyst prepared with those reported in the literature.

Catalysts	Reaction conditions	T (°C)	TOF × 10 ¹⁰ (mol m _{cat} ⁻² s ⁻¹)	Selectivity to CO ₂ ^a (%)	Reference
NiCeO _x -4	0.2% C ₃ H ₈ , 2% O ₂ , 97.8% Ar	250	12.37	> 99	This work
Pd/ZSM-5	0.2% C ₃ H ₈ , 2% O ₂ , 97.8% N ₂	280	0.43	–	[7]
Mn-doped ZrO ₂ (Mn/Zr = 1:4)	0.9% C ₃ H ₈ , 99.1% air	350	2.63	–	[66]
Co-doped ZrO ₂ (Co/Zr = 1:4)	0.9% C ₃ H ₈ , 99.1% air	350	6.97	–	[66]
NiO	0.8% C ₃ H ₈ , 99.2% air	225	5.87	94.0	[67]
NiCe (Ni/Ce = 1:1)	0.8% C ₃ H ₈ , 99.2% air	225	6.94	94.3	[67]

^a when the propane conversion is 50%.

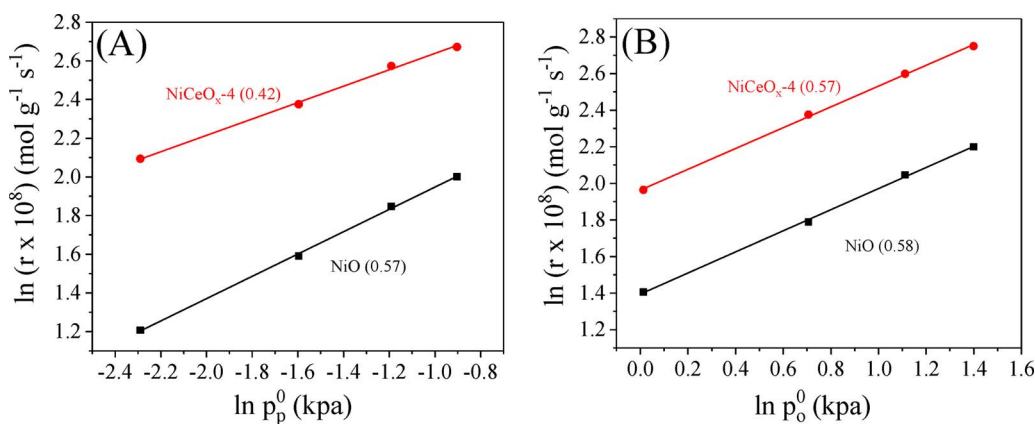


Fig. 3. Dependence of propane oxidation (r) on (A) propane and (B) the oxygen partial pressure (P) over the NiO and NiCeO_x-4 catalysts.

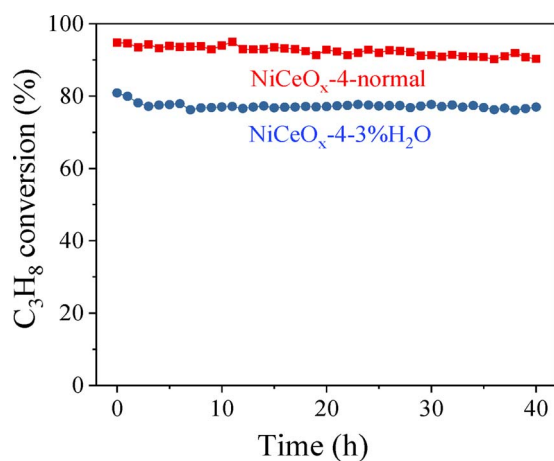


Fig. 4. Effect of vapour in the reactant gas on the catalytic stability of the NiCeO_x-4 catalyst at 300 °C. (The feed gas was 0.2% C₃H₈ + 2% O₂ + (or 3% H₂O)/Ar, and the GHSV was 30000 mL h⁻¹ g_{cat}⁻¹).

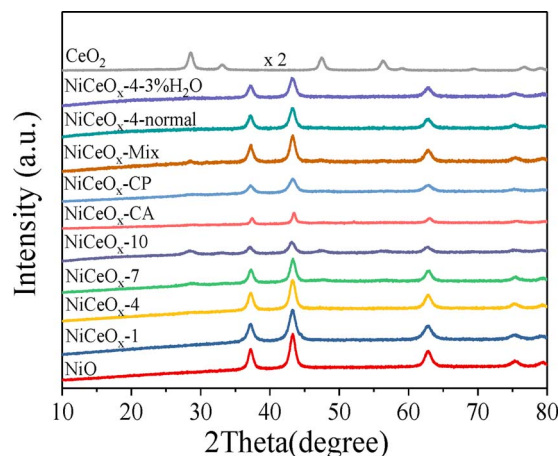


Fig. 5. XRD patterns of CeO₂, NiO and NiCeO_x catalysts.

3.2.3. Raman spectra

Fig. 8 shows the Raman spectra of the NiCeO_x catalysts. For pure CeO₂, there is a strong band at 462 cm⁻¹ and two weak bands at 598 and 1175 cm⁻¹, which are assigned to the fluorite F_{2g} mode, defect-induced (D) mode and second-order longitudinal optical (2LO) mode, respectively [43,44]. For pure NiO, the broad band that is assigned to the Ni-O stretching mode in NiO appeared at 500 cm⁻¹ [42,45,46]. With the incorporation of ceria, a new band at 639 cm⁻¹ was found for the NiCeO_x-4 catalyst, which may be caused by the Ni-O-Ce interaction [47,48]. Furthermore, the bands that correspond to CeO₂ were absent

in the Raman spectrum of the NiCeO_x-4 catalyst due to an overlap with the NiO absorption bands. Amongst the NiCeO_x catalysts prepared with various methods, the Raman spectrum of the NiCeO_x-Mix catalyst was similar with that of the NiCeO_x-4 catalyst. However, the Raman spectra of the NiCeO_x-CA and NiCeO_x-CP catalysts are different from that of the NiCeO_x-4 catalyst, in which the intensity of absorption bands obviously decreased and the broad band shifted from 500 to 520 cm⁻¹. The results show that the lattice distortion of the NiCeO_x-CA and NiCeO_x-CP catalysts is more critical than that of the NiCeO_x-4 catalyst, due to the modification of the Ni-O bonding symmetry stemming from the presence of Ce in NiO [49,50].

3.2.4. XPS

Fig. 9A shows Ni 2p_{3/2} XPS spectra of the pure NiO and NiCeO_x catalysts prepared using different methods. The signal can be decomposed into four Gaussian-Lorentzian peaks. The peak at 853.2 eV was assigned to the Ni²⁺ species on catalyst surface [36,42], whereas the peak at 855.1 eV was interpreted as the nonlocal screening of the 2p hole in the NiO structure [36]. The satellites at 860.4 and 864.1 eV were attributed to Ni²⁺ compounds, such as Ni(OH)₂ or NiO species [36]. In contrast, the peak assigned to the Ni³⁺ species was absent [51]. Since the intensity of the peak at 855.1 eV was sensitive to the structural arrangement and the nature of Ni²⁺ that surrounded the atoms, the peak area ratio between the peaks at 855.1 and 853.2 eV was calculated. The results suggest that the ratio for pure NiO (1.85) is lower than that of the NiCeO_x-4 catalyst (2.25), which indicates that the proportion of Ni²⁺ defects in the NiCeO_x catalyst is higher than that in pure NiO due to the formation of NiCeO_x nanoparticles by the incorporation of Ni into the CeO₂ nanoparticles.

Fig. 9B shows the O 1s XPS spectra of the pure NiO and NiCeO_x catalysts prepared using different methods. All the catalysts displayed two peaks at 529 and 531 eV, which were assigned to lattice oxygen (O²⁻) and surface oxygen (O⁻), respectively [36,52,53]. The relative intensities of these two peaks for NiO and NiCeO_x catalysts are ordered as follows: NiCeO_x-4 (0.53) > NiCeO_x-CP (0.48) > NiCeO_x-CA (0.44) > NiCeO_x-Mix (0.42) > NiO (0.36). This ordering indicates that ceria incorporation into NiO can modify the chemical state of the oxygen species at the surface or subsurface.

3.2.5. H₂-TPR and C₃H₈-TPSR profile

Fig. 10 shows the H₂-TPR profiles of CeO₂, NiO and NiCeO_x catalysts prepared with different methods. For pure CeO₂, two weak reduction peaks centred at approximately 380 °C and 750 °C are present, which can be attributed to the reduction of surface oxygen species and the bulk lattice oxygen of ceria, respectively [37]. The pure NiO and NiCeO_x-Mix catalysts exhibited a main reduction peak at ~310 °C, which was assigned to the reduction of Ni²⁺ species to metallic nickel [54,55]. However, for the NiCeO_x-4 catalyst, the H₂-TPR signal can be decomposed to three peaks. In addition to the reduction peak at ~310 °C, a

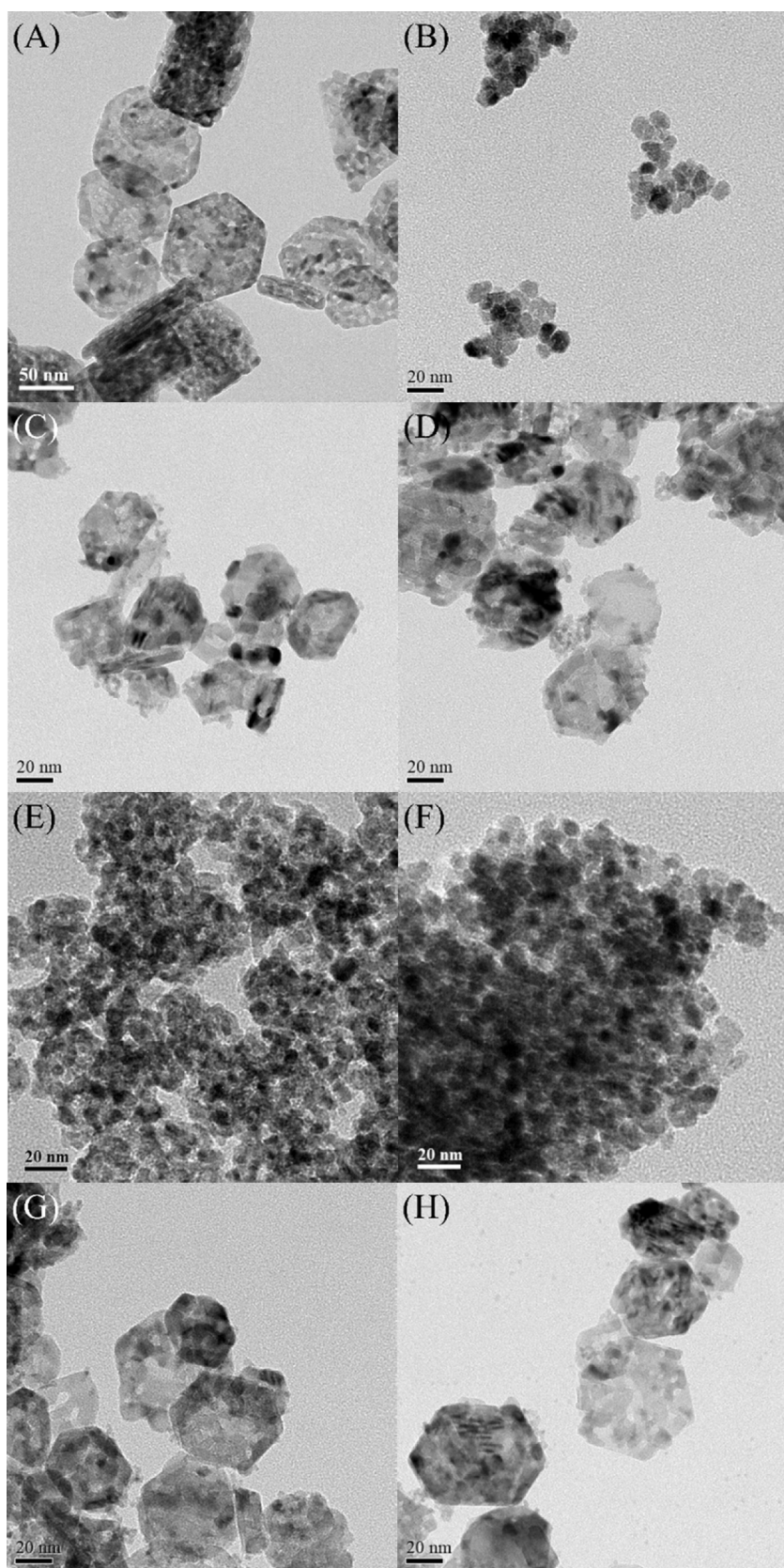


Fig. 6. TEM images of (A) NiO, (B) CeO₂, (C) NiCeO_x-4, (D) NiCeO_x-7, (E) NiCeO_x-CP and (F) NiCeO_x-CA catalysts.

new reduction peak centred at $\sim 340^\circ\text{C}$ and a small peak at 250°C appeared, which was assigned to the reduction of Ni^{2+} species with a strong interaction with Ce [56,57] and adsorbed oxygen species in CeO₂ [58], respectively. As for the NiCeO_x-CA and NiCeO_x-CP catalysts, the

corresponding reduction peaks shifted to a higher temperature compared with that of the NiCeO_x-4 catalyst, which indicates that the preparation methods strongly affected the reducibility of NiCeO_x composite oxide. The NiCeO_x catalyst that was prepared using the

Table 3The grain size, lattice parameter, and BET surface area (S_{BET}) of NiCeO_x catalyst.

Catalyst	Theoretical Ce/(Ce + Ni) molar ratio	Actual Ce/(Ce + Ni) molar ratio ^a	S_{BET} (m^2/g)	Grain size (nm) ^b	NiO lattice parameter (nm)	CeO_2 lattice parameter (nm)
CeO_2	1	1	82	10.9	–	0.5405
$\text{NiCeO}_x\text{-1}$	0.01	0.0094	84	14.7	0.4179	–
$\text{NiCeO}_x\text{-4}$	0.04	0.0328	87	13.0	0.4177	–
$\text{NiCeO}_x\text{-7}$	0.07	0.0607	98	13.3	0.4179	–
$\text{NiCeO}_x\text{-10}$	0.1	0.0891	110	11.8	0.4180	0.5353
NiO	0	0	75	17.5	0.4178	–
$\text{NiCeO}_x\text{-CP}$	0.04	0.0312	101	4.0	0.4177	–
$\text{NiCeO}_x\text{-CA}$	0.04	0.0331	29	54.6	0.4176	–
$\text{NiCeO}_x\text{-Mix}$	0.04	0.0355	78	14.5	0.4179	–

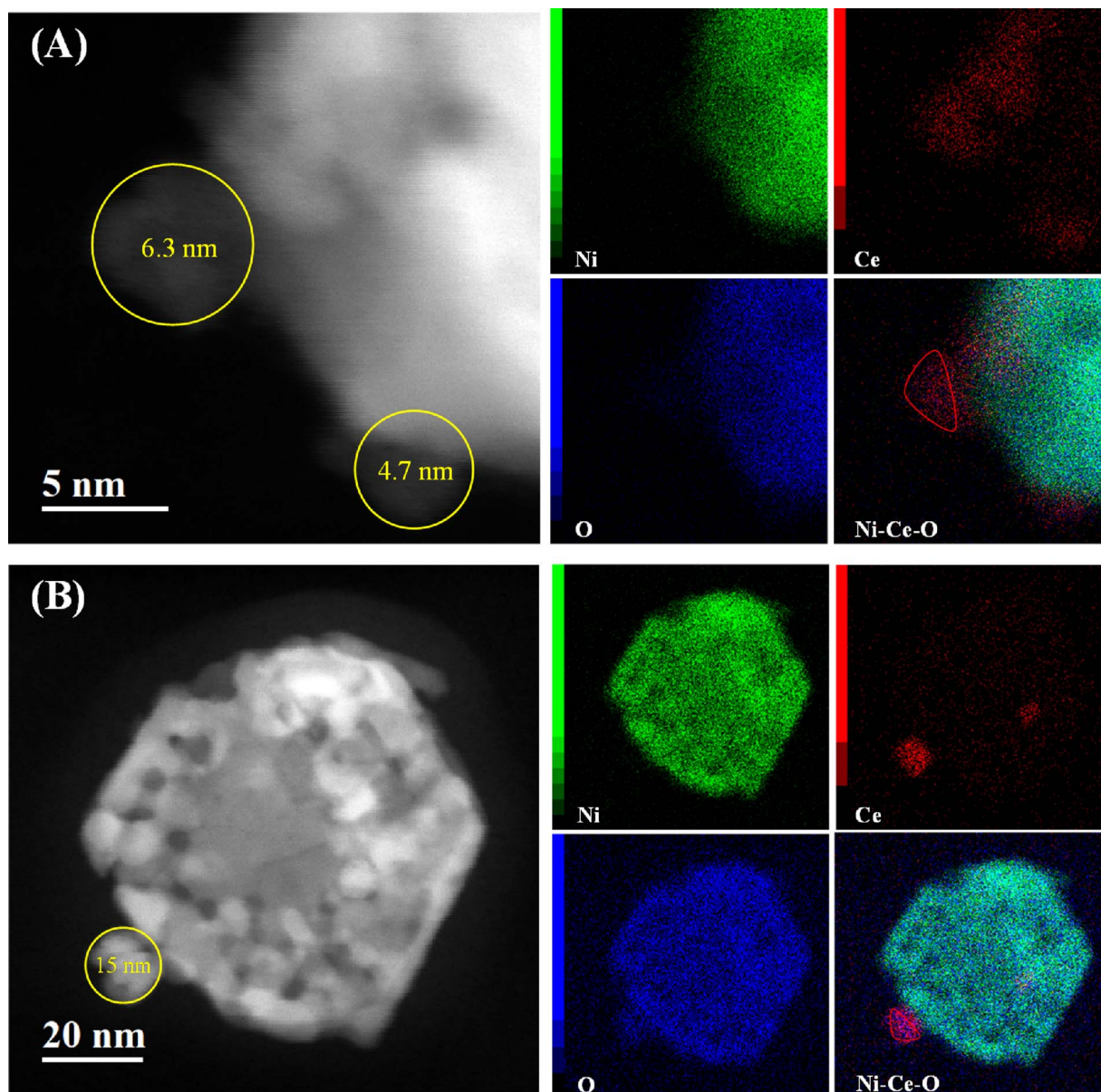
^a Detected by ICP-AES.^b Calculated by the XRD patterns using the Williamson-Hall method.**Table 4**

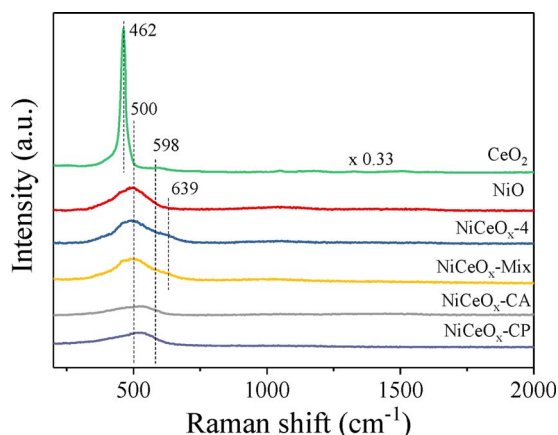
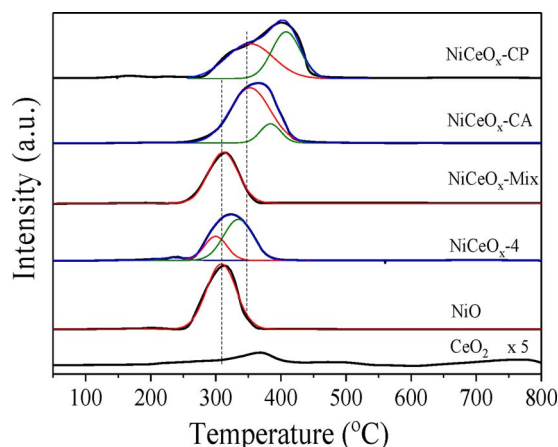
The Ce, Ni and O concentrations in the selected regions that were marked by a red triangle in Fig. 7.

Catalysts	Ce concentration		Ni concentration		O concentration	
	wt%	wt% Sigma	wt%	wt% Sigma	wt%	wt% Sigma
$\text{NiCeO}_x\text{-4}$	75.66	3.55	9.47	1.11	14.87	1.37
$\text{NiCeO}_x\text{-Mix}$	76.40	2.96	0	0	23.60	0.60

hydrothermal method contained more easily reduced species than that of $\text{NiCeO}_x\text{-CA}$ and $\text{NiCeO}_x\text{-CP}$, which is promising for improved catalytic activity for propane combustion.

Fig. 11 shows the C_3H_8 -TPSR results for the NiO and NiCeO_x catalysts. Because CO_2 and C_3H_8 have the same mass number, both the MS signals of $m/z = 44$ (CO_2 or propane) and 43 (propane) were simultaneously recorded. For pure NiO , a positive peak centred at approximately 330°C was found for the MS signals of $m/z = 44$. Since a negative peak was presented at the corresponding position for the MS signals of $m/z = 43$, the positive peak for the MS signals of $m/z = 44$

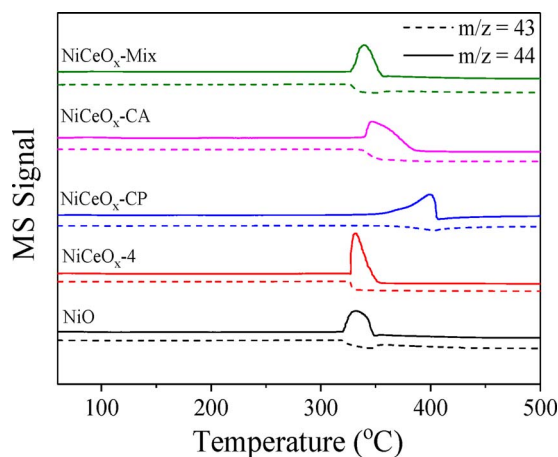
**Fig. 7.** HAADF-STEM images and EELS elemental mapping imagery of the $\text{NiCeO}_x\text{-4}$ (A) and $\text{NiCeO}_x\text{-Mix}$ (B) catalysts.

Fig. 8. Raman spectra of CeO₂, NiO and NiCeO_x catalysts.Fig. 10. H₂-TPR profiles of the NiO, CeO₂ and NiCeO_x catalysts.

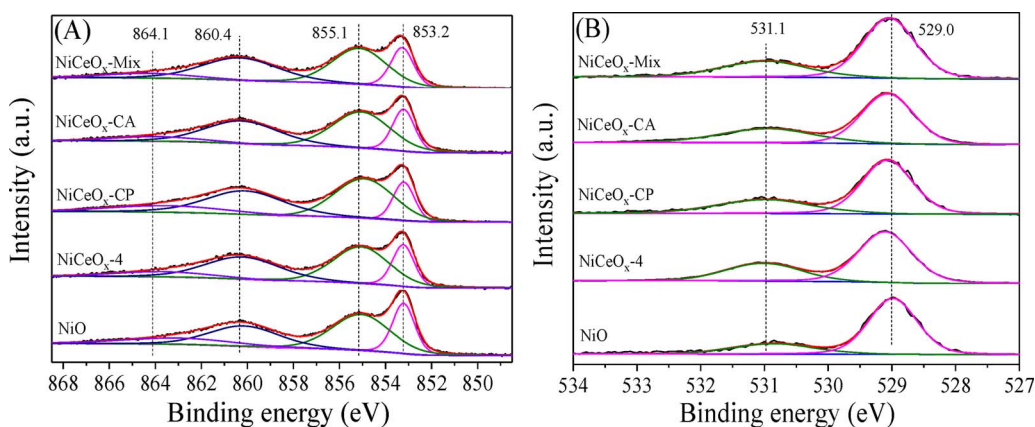
was attributed to CO₂ that was produced from the total oxidation of propane instead of propane desorption from the catalysts. Similar results were found on the other catalysts, but the CO₂ peak from the NiCeO_x-CP and NiCeO_x-CA catalysts shifted to a higher temperature, which indicates a low performance for propane activation. This result is in agreement with the weak reducibility of the NiCeO_x-CP and NiCeO_x-CA catalysts that were shown in the H₂-TPR results. Additionally, the amount of CO₂ detected on the different catalysts follows the sequence: NiCeO_x-4 > NiCeO_x-CP > NiCeO_x-CA > NiCeO_x-Mix > NiO. These results revealed that the NiCeO_x-4 catalyst possessed more active oxygen species than the pure NiO and other NiCeO_x catalysts, whereas the NiCeO_x-Mix catalyst has the least amount of active oxygen species amongst the NiCeO_x catalysts that were prepared with different methods. This order is consistent with their catalytic activity for the complete oxidation of propane.

3.2.6. O₂-TPD

Fig. 12 shows the O₂-TPD-MS curves for the NiO and NiCeO_x catalysts. The pure NiO catalyst presents a main desorption peak that is centred at approximately 400 °C and assigned to the desorption of O[−] species [59]. The NiCeO_x-4 catalyst exhibits a desorption curve that is similar to that of the NiO catalyst in the temperature range 350–450 °C but the desorption peak intensity is significantly higher than the latter. A similar desorption curve is also present with the NiCeO_x-CP catalyst but the desorption temperature increased from 400 to 450 °C. In contrast, two overlapping desorption peaks at 350–450 °C are present when using the NiCeO_x-CA and NiCeO_x-Mix catalysts, which can be assigned to the O[−] species on different sites. According to the calculation of the area of desorption peak for different catalysts in Fig. 12, it can be deduced that the amount of O[−] desorption follows the sequence: NiCeO_x-

Fig. 11. C₃H₈-TPSR experiments over the NiO and NiCeO_x catalysts at 300 °C.

4 > NiCeO_x-CA > NiCeO_x-CP > NiCeO_x-Mix > NiO, which is consistent with the O 1s XPS results. Additionally, amongst the different catalysts, the initial desorption temperature of the O[−] desorption peak was the lowest on NiCeO_x-4 and the highest on NiCeO_x-CP. Compared with the C₃H₈-TPSR results, the O[−] desorption temperature is close to propane surface reaction temperature, which indicates that the CO₂ desorption peak in Fig. 12 can be related to the consumption of O[−] species, i.e., the O[−] species can take part in the reaction. As a result, the NiCeO_x-4 catalyst possessed a high oxygen adsorption capability and these oxygen species can be desorbed at a low temperature, which is favourable for high catalytic activity for propane combustion.

Fig. 9. XPS of Ni 2p_{3/2} (A) and O 1s (B) for the NiO and NiCeO_x catalysts.

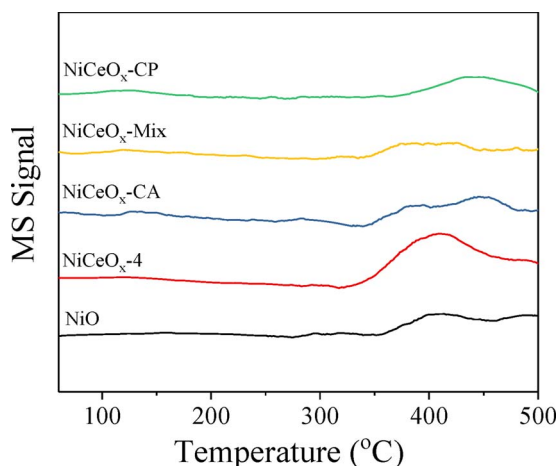


Fig. 12. O₂-TPD-MS experiment over the NiO and NiCeO_x catalysts at 300 °C.

3.2.7. In situ DRIFT spectra for surface reaction

Fig. 13 shows the DRIFTS data of the C₃H₈ + O₂ reaction over the CeO₂, NiO and NiCeO_x-4 catalysts at 300 °C. For pure CeO₂, when the feed gas of 0.5% C₃H₈ + 5% O₂/Ar was purged in the chamber for 30 min, absorption bands at 2967, 2931 and 2840 cm⁻¹ were detected and assigned to $\nu_{as}(\text{CH}_3)$, $\nu_{as}(\text{CH}_2)$ and $\nu_s(\text{CH}_2)$, respectively [60–63]. Furthermore, multiple absorption bands assigned to the carboxylate species were present between 1700 and 1200 cm⁻¹ (the details are listed in Table 5), which indicates that propane can be partially oxidized and then adsorbed on the CeO₂ surface, which is consistent with our previous results [44]. After desorption at 300 °C for 30 min, the absorption bands at 2931 and 2840 cm⁻¹ that correspond to chemically adsorbed propane were maintained but the absorption band at 2967 cm⁻¹ that corresponds to gaseous propane disappeared, which

Table 5

Frequencies of functional groups present on different catalysts analyzed by DRIFTS.

Mode (wave number cm ⁻¹)	Infrared band wavenumber (cm ⁻¹)				References
	NiO	NiCeO _x -4	NiCeO _x -Mix	CeO ₂	
$\nu_{as}(\text{CH}_3)$	2967	2967	2967	2967	[60–63]
$\nu_{as}(\text{CH}_2)$				2931	
$\nu_s(\text{CH}_2)$		2863		2840	
$\nu(\text{CO}_2)$	2200–2400	2200–2400	2200–2400		[62–65]
$\nu_{as}(\text{C}=\text{C})$		1617			
$\nu_{as}(\text{COO})$	1521	1522	1525	1544	
				1500	[62,63,68]
$\delta_{as}(\text{CH}_3)$	1434	~1473	1477	~1460	
$\delta_s(\text{CH}_3)$	1346	1376	1371	1371	
		1326	1328	1356	[62,63,69]
$\nu(\text{C}-\text{O})$		1275	1261	1295	
$\delta(\text{CH})$		1222		1222	

indicates that propane was strongly adsorbed on the ceria surface. Moreover, the intensity of absorption bands at 1200–1700 cm⁻¹ hardly changed, which indicates that the partially oxidized species also strongly bonded on the ceria surface.

In the DRIFTS spectra of the C₃H₈ + O₂ reaction over pure NiO, three main absorption bands were present at 1521, 1434 and 1346 cm⁻¹, which can be attributed to $\nu_{as}(\text{COO})$, $\delta_{as}(\text{CH}_3)$ and $\delta_s(\text{CH}_3)$, respectively (Table 5). Additionally, there was an absorption band at 2339 cm⁻¹ that was assigned to gaseous CO₂, which originated from the reaction between C₃H₈ and O₂ under the conditions of DRIFTS spectra. After desorption at 300 °C for 30 min, the absorption band at 2339 cm⁻¹ that corresponded to gaseous CO₂ disappeared and the intensity of all absorption bands in the range of 1300–1550 cm⁻¹ slightly decreased, which suggests that the partially oxidized species also strongly bonded on the NiO surface.

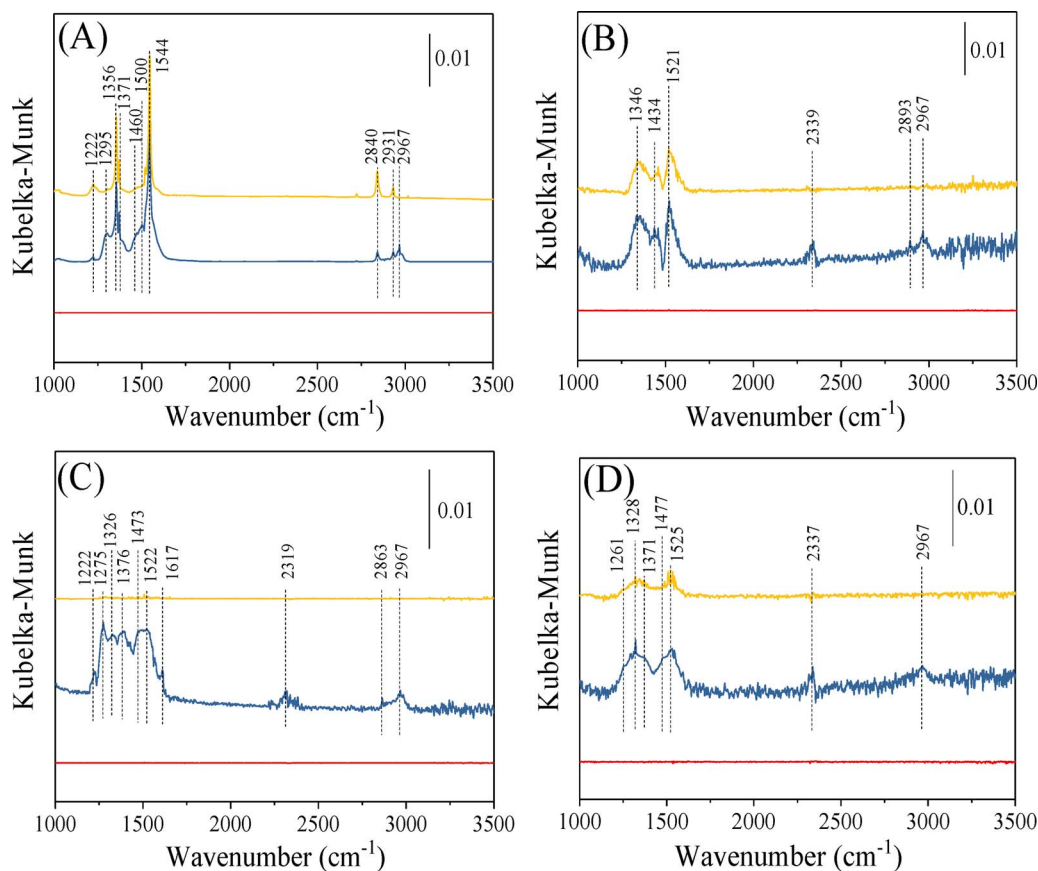
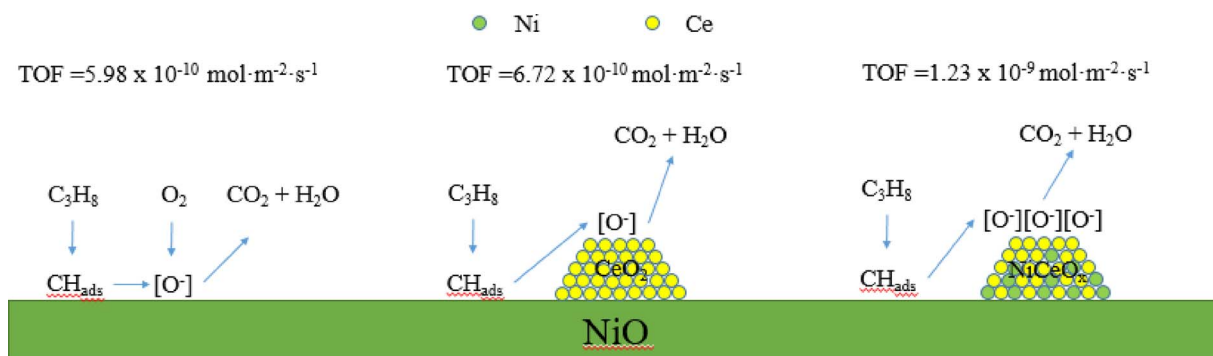


Fig. 13. DRIFT spectra of the 0.5% C₃H₈ + 5% O₂/Ar reaction (blue line) and desorption (yellow line) on CeO₂ (A), NiO (B), NiCeO_x-4 (C) and NiCeO_x-Mix (D) catalysts at 300 °C. The feed gas (25 mL/min) consisted of 0.5% C₃H₈, 5% O₂ and 94.5% Ar. All spectra were gathered after the samples were treated under atmospheric conditions for 30 min (For interpretation of the references to colour in this figure legend, the reader is referred to the web version of this article.)



Scheme 1. Reaction model of propane combustion over catalysts.

The DRIFTS spectra of the $\text{C}_3\text{H}_8 + \text{O}_2$ reaction over the NiCeO_x -4 and NiCeO_x -Mix catalysts are similar to the results over pure NiO . However, a new absorption band was found at 1617 cm^{-1} over the NiCeO_x -4 catalyst that was assigned to $\nu_{\text{as}}(\text{C}=\text{C})$ [62–65], and indicated an enhancement in the ability to break the C–H bond of propane. Moreover, the absorption bands that correspond to partially oxidized species and the band that corresponds to gaseous CO_2 disappeared after desorption at 300°C for 30 min. This result showed that the partially oxidized species were immediately removed from the surface of the NiCeO_x -4 catalyst during the desorption process. As a result, the active sites were exposed again, which led to an improvement in its catalytic performance for propane combustion. In contrast, the bands that corresponded to the partially oxidized species were still present over the NiCeO_x -Mix catalyst after desorption at 300°C for 30 min, which indicates that the partially oxidized species cannot be removed from the surface of the NiCeO_x -Mix catalyst during the desorption process.

3.3. Discussion

NiCeO_x mixed oxide exhibited more catalytic activity for propane combustion than pure NiO and its catalytic activity was dependent on the composition and preparation methods. Amongst the NiCeO_x catalysts that were prepared using the hydrothermal method, the NiCeO_x -4 catalyst exhibited the highest catalytic activity and the TOF value of the NiCeO_x -4 catalyst was twice that of pure NiO . The H_2 -TPR results showed that the incorporation of ceria into NiO markedly improved the reducibility of the NiCeO_x -4 catalyst. The C_3H_8 -TPSR results confirmed that the NiCeO_x -4 catalyst possessed more active oxygen species to take part in the reaction of propane combustion compared with pure NiO . The O 1s XPS and O_2 -TPD results further support this conclusion. Furthermore, *in situ* DRIFTS spectra over the pure NiO and CeO_2 , NiCeO_x -4 and NiCeO_x -Mix catalysts revealed that the NiCeO_x -4 catalyst possessed a superior ability to break the C–H bond of propane. Note that propane combustion follows the Mars-van Krevelen redox mechanism on NiO -based catalysts [35,36,66]. Therefore, compared with pure NiO , the enhancement in the catalytic performance of the NiCeO_x -4 catalyst for propane combustion can be explained by an improvement in reducibility, an increase in the amount of reactive oxygen species and an enhancement in the ability to break the C–H bond of propane.

To further evaluate the relationship between the structure of the NiCeO_x -4 catalyst and its catalytic activity, the NiCeO_x -Mix catalyst was also prepared by directly mixing pure NiO and CeO_2 powders. The results showed that the TOF of the NiCeO_x -Mix catalyst ($6.72 \times 10^{-10}\text{ mol m}^{-2}\text{ s}^{-1}$) was significantly lower than that of the NiCeO_x -4 catalyst ($12.37 \times 10^{-10}\text{ mol m}^{-2}\text{ s}^{-1}$). Based on the XRD results and HAADF-STEM images, the NiCeO_x -Mix catalyst consists of pure CeO_2 nanoparticles with a size of $\sim 15\text{ nm}$ and is supported on NiO , whereas CeO_2 exists as NiCeO_x nanoparticles with a size of 5–6 nm and is supported on NiCeO_x -4 catalysts. Therefore, all the results of Raman, XPS, H_2 -TPR, C_3H_8 -TPSR, O_2 -TPD and *in situ* DRIFT spectra of

the $\text{C}_3\text{H}_8 + \text{O}_2$ reaction over the NiCeO_x -Mix catalyst are close to that of pure NiO , which indicates the existence of a synergistic effect of NiO and CeO_2 in the NiCeO_x -4 catalyst due to its specific structure, as shown in Scheme 1. Particularly, NiCeO_x nanoparticles that were located on the NiO nanosheet surface are the main reason for its high catalytic activity.

However, an increase in the Ce content of the NiCeO_x catalysts, which were prepared by the hydrothermal method, led to a decrease in the catalytic activity of the NiCeO_x -7 and NiCeO_x -10 catalysts for propane combustion. XRD results indicated that the diffraction peaks of ceria appeared when the $\text{Ce}/(\text{Ce} + \text{Ni})$ molar ratio of the NiCeO_x catalysts was increased to 7% and 10%. TEM results showed that the morphology of the NiCeO_x -7 catalyst changed from a hexagonal nanosheet to an irregular shape. Regarding the low activity of pure CeO_2 for propane combustion, the CeO_2 crystals that form on the surface of the NiCeO_x -7 and NiCeO_x -10 catalysts can block the active sites, which results in the low catalytic activity for propane combustion.

Additionally, the preparation method also seriously affected the catalytic activities of NiCeO_x catalysts. The NiCeO_x -4 catalyst that was prepared using the hydrothermal method exhibited better catalytic activity than those of the NiCeO_x -CP and NiCeO_x -CA catalysts. The XPS, H_2 -TPR, C_3H_8 -TPSR, O_2 -TPD characterization results and *in situ* DRIFT spectra of the $\text{C}_3\text{H}_8 + \text{O}_2$ reaction revealed that the NiCeO_x -4 catalyst had strong reducibility, a large number of active oxygen species, and strong ability to break the C–H bond of propane, which led to its higher catalytic activity for propane combustion compared with the NiCeO_x -CP and NiCeO_x -CA catalysts.

4. Conclusions

In summary, Ni-Ce-O mixed metal oxide catalysts were prepared using hydrothermal methods and showed a highly efficient for total oxidation of propane. The appropriate molar ratio of $\text{Ce}/(\text{Ce} + \text{Ni})$ is 4%. The TOF value of NiCeO_x -4 at 250°C is $1.24 \times 10^{-9}\text{ mol m}^{-2}\text{ s}^{-1}$, which is twice as much as it of pure NiO . Besides, the NiCeO_x -4 samples also demonstrated a good thermal stability and water resistance for total oxidation of propane. The presence of ceria strongly affected the crystal structure, surface phase composition and reducibility of NiCeO_x catalysts.

The preparation method strongly affected the morphology, crystallinity, reducibility and surface composition of NiCeO_x catalysts. The NiCeO_x -4 catalyst prepared by hydrothermal method presented hexagonal nanosheet shape and CeO_2 was existed as NiCeO_x nanoparticles supported on the NiCeO_x -4 catalysts. The presence of NiCeO_x nanoparticles not only provided more reactive O^- species but also enhanced the reducibility based on the synergistic effect of CeO_2 and NiO . In addition, this special structure can inhibit the accumulation of carboxylate related species and enhance the ability to break C–H bond of propane during the reaction. Therefore, the NiCeO_x -4 catalyst showed the higher catalytic activity for total oxidation of propane, compared

with the NiCeO_x-CP, NiCeO_x-CA and NiCeO_x-Mix catalysts.

Acknowledgements

This work was supported financially by the National Key Research and Development Program of China (2016YFC0204300), the National Natural Science Foundation of China (21577034), the Science and Technology Commission of Shanghai Municipality (16ZR1407900) and the Fundamental Research Funds for the Central Universities (222201717003).

References

- [1] L.F. Liotta, Appl. Catal. B: Environ. 100 (2010) 403–412.
- [2] K. Ji, H. Dai, J. Deng, L. Song, B. Gao, Y. Wang, X. Li, Appl. Catal. B: Environ. 129 (2013) 539–548.
- [3] Y. Liu, H. Dai, Y. Du, J. Deng, L. Zhang, Z. Zhao, Appl. Catal. B: Environ. 119 (2012) 20–31.
- [4] M. Magureanu, D. Piroi, N.B. Mandache, V.I. Parvulescu, V. Parvulescu, B. Cojocaru, C. Cadigan, R. Richards, H. Daly, C. Hardacre, Appl. Catal. B: Environ. 104 (2011) 84–90.
- [5] T.F. Garetto, E. Rincón, C.R. Apesteguía, Appl. Catal. B: Environ. 73 (2007) 65–72.
- [6] V.R. Choudhary, G.M. Deshmukh, S.G. Pataskar, Environ. Sci. Technol. 39 (2005) 2364–2368.
- [7] Z.Z. Zhu, G.Z. Lu, Z.G. Zhang, Y. Guo, Y.L. Guo, Y.Q. Wang, ACS Catal. 3 (2013) 1154–1164.
- [8] B. Solsona, E. Aylon, R. Murillo, A.M. Mastral, A. Monzonis, S. Agouram, T.E. Davies, S.H. Taylor, T. Garcia, J. Hazard Mater. 187 (2011) 544–552.
- [9] B.H. Aristizabal, C.M. de Correa, A.I. Serykh, C.E. Hetrick, M.D. Amiridis, J. Catal. 258 (2008) 95–102.
- [10] M. Cargnello, J.D. Jaén, J.H. Garrido, K. Bakhmutsky, T. Montini, J.C. Gámez, R. Gorte, P. Fornasiero, Science 337 (2012) 713–717.
- [11] Z.Z. Zhu, G.Z. Lu, Y. Guo, Y.L. Guo, Z.G. Zhang, Y.Q. Wang, X.Q. Gong, Chemcatchem 5 (2013) 2495–2503.
- [12] S. Chen, Y.H. Li, F. Ma, F. Chen, W.M. Lu, Catal. Sci. Technol. 5 (2015) 1213–1221.
- [13] W.B. Li, J.X. Wang, H. Gong, Catal. Today 148 (2009) 81–87.
- [14] W. Zhan, Q. He, X. Liu, Y. Guo, Y. Wang, L. Wang, Y. Guo, A.Y. Borisevich, J. Zhang, G. Lu, S. Dai, J. Am. Chem. Soc. 138 (2016) 16130–16139.
- [15] W. Zhan, Y. Shu, Y. Sheng, H. Zhu, Y. Guo, L. Wang, Y. Guo, J. Zhang, G. Lu, S. Dai, Angew. Chem. Int. Ed. 56 (2017) 4494–4498.
- [16] W. Zhan, J. Wang, H. Wang, J. Zhang, X. Liu, P. Zhang, M. Chi, Y. Guo, Y. Guo, G. Lu, S. Sun, S. Dai, H. Zhu, J. Am. Chem. Soc. 139 (2017) 8846–8854.
- [17] G. Jones, J.G. Jakobsen, S.S. Shim, J. Kleis, M.P. Andersson, J. Rossmel, F. Abild-Pedersen, T. Bligaard, S. Helveg, B. Hinnemann, J.R. Rostrup-Nielsen, I. Chorkendorff, J. Sehested, J.K. Nørskov, J. Catal. 259 (2008) 147–160.
- [18] J. Rostrup-Nielsen, J.B. Hansen, J. Catal. 144 (1993) 38–49.
- [19] D. Qin, J. Lapszewicz, Catal. Today 21 (1994) 551–560.
- [20] P. Ferrin, D. Simonetti, S. Kandoi, E. Kunkes, J.A. Dumesic, J.K. Nørskov, M. Mavrikakis, J. Am. Chem. Soc. 131 (2009) 5809–5815.
- [21] Z. Liu, D.C. Grinter, P.G. Lustemberg, T.D. Nguyen-Phan, Y. Zhou, S. Luo, I. Waluyo, E.J. Crumlin, D.J. Stacchiola, J. Zhou, J. Carrasco, H.F. Busnengo, M.V. Ganduglia-Pirovano, S.D. Senanayake, J.A. Rodriguez, Angew. Chem. Int. Ed. 55 (2016) 7455–7459.
- [22] Z. Skoufa, E. Heracleous, A.A. Lemonidou, J. Catal. 322 (2015) 118–129.
- [23] M.H. Mahyuddin, A. Staykov, Y. Shiota, K. Yoshizawa, ACS Catal. 6 (2016) 8321–8331.
- [24] V. Choudhary, K. Mondal, T. Choudhary, Appl. Catal. A: Gen. 306 (2006) 45–50.
- [25] B. Yang, R. Burch, C. Hardacre, G. Headdock, P. Hu, ACS Catal. 2 (2012) 1027–1032.
- [26] M. Tanaka, Y. Tsujimoto, T. Miyazaki, M. Warashina, S. Wakamatsu, Chemosphere-Global Change Sci. 3 (2001) 185–197.
- [27] J. Okal, M. Zawadzki, W. Tylus, Appl. Catal. B: Environ. 101 (2011) 548–559.
- [28] J.E. Park, K.B. Kim, Y.A. Kim, K.S. Song, E.D. Park, Catal. Lett. 143 (2013) 1132–1138.
- [29] D.P. Debecker, B. Farin, E.M. Gaigneaux, C. Sanchez, C. Sasse, Appl. Catal. A: Gen. 481 (2014) 11–18.
- [30] M.N. Taylor, W. Zhou, T. Garcia, B. Solsona, A.F. Carley, C.J. Kiely, S.H. Taylor, J. Catal. 285 (2012) 103–114.
- [31] T. Garetto, E. Rincón, C. Apesteguía, Appl. Catal. B: Environ. 48 (2004) 167–174.
- [32] T. Kanazawa, Appl. Catal. B: Environ. 65 (2006) 185–190.
- [33] M.R. Morales, B.P. Barbero, L.E. Cadus, Appl. Catal. B: Environ. 74 (2007) 1–10.
- [34] B. Puértolas, A. Smith, I. Vázquez, A. Dejoz, A. Moragues, T. Garcia, B. Solsona, J. Chem. Eng. 229 (2013) 547–558.
- [35] I. Yuranov, N. Dunand, L. Kiwi-Minsker, A. Renken, Appl. Catal. B: Environ. 36 (2002) 183–191.
- [36] V.V. Kaichev, D. Teschner, A.A. Saraev, S.S. Kosolobov, A.Y. Gladky, I.P. Prosvirin, N.A. Rudina, A.B. Ayupov, R. Blume, M. Havecker, A. Knop-Gericke, R. Schlögl, A.V. Latyshev, V.I. Bukhtiyarov, J. Catal. 334 (2016) 23–33.
- [37] A. Trovarelli, Catal. Rev. 38 (1996) 439–520.
- [38] Z. Yan, Z. Xu, J. Yu, M. Jaroniec, Appl. Catal. B: Environ. 199 (2016) 458–465.
- [39] T. Li, G. Xiang, J. Zhuang, X. Wang, Chem. Commun. 47 (2011) 6060–6062.
- [40] M. Retuerto, A.G. Pereira, F.J. Pérez-Alonso, M.A. Peña, J.L.G. Fierro, J.A. Alonso, M.T. Fernández-Díaz, L. Pascual, S. Rojas, Appl. Catal. B: Environ. 203 (2017) 363–371.
- [41] E. Rombi, M.G. Cutrufello, L. Atzori, R. Monaci, A. Ardu, D. Gazzoli, P. Deiana, I. Ferino, Appl. Catal. A: Gen. 515 (2016) 144–153.
- [42] B. Solsona, P. Concepcion, S. Hernandez, B. Demicol, J.M.L. Nieto, Catal. Today 180 (2012) 51–58.
- [43] W. Weber, K. Hass, J. McBride, Phys. Rev. B 48 (1993) 178–185.
- [44] Z. Hu, X.F. Liu, D.M. Meng, Y. Guo, Y.L. Guo, G.Z. Lu, ACS Catal. 6 (2016) 2265–2279.
- [45] E. Heracleous, A.A. Lemonidou, J. Catal. 237 (2006) 162–174.
- [46] B. Savova, S. Lorient, D. Filkova, J.M.M. Millet, Appl. Catal. A: Gen. 390 (2010) 148–157.
- [47] P. Brussino, J. Bortolozzi, V. Milt, E. Banús, M. Ulla, Catal. Today 273 (2016) 259–265.
- [48] Y.M. Liu, L.C. Wang, M. Chen, J. Xu, Y. Cao, H.Y. He, K.N. Fan, Catal. Lett. 130 (2009) 350–354.
- [49] X.J. Du, D.S. Zhang, L.Y. Shi, R.H. Gao, J.P. Zhang, J. Phys. Chem. C 116 (2012) 10009–10016.
- [50] K.C. Verma, R.K. Kotnala, J. Solid State Chem. 246 (2017) 150–159.
- [51] A. Carley, S. Jackson, J. O'shea, M. Roberts, Surf. Sci. 440 (1999) L868–L874.
- [52] C. Rao, V. Vijayakrishnan, G. Kulkarni, M. Rajumon, Appl. Surf. Sci. 84 (1995) 285–289.
- [53] M. Hegde, M. Ayyoob, Surf. Sci. 173 (1986) L635–L640.
- [54] T. Takeguchi, S.N. Furukawa, M. Inoue, J. Catal. 202 (2001) 14–24.
- [55] J. Richardson, B. Turk, M. Twigg, Appl. Catal. A: Gen. 148 (1996) 97–112.
- [56] L. Pino, A. Vita, F. Cipiti, M. Lagana, V. Recupero, Catal. Lett. 122 (2008) 121–130.
- [57] S. Xu, X. Yan, X. Wang, Fuel 85 (2006) 2243–2247.
- [58] C. Tang, B. Sun, J. Sun, X. Hong, Y. Deng, F. Gao, L. Dong, Catal. Today 281 (2017) 575–582.
- [59] M. Iwamoto, Y. Yoda, M. Egashira, T. Seiyama, J. Phys. Chem. 80 (1976) 1989–1994.
- [60] M. Hasan, M. Zaki, L. Pasupulety, J. Phys. Chem. B 106 (2002) 12747–12756.
- [61] B. Wang, X.D. Wu, R. Ran, Z.C. Si, D. Weng, J. Mol. Catal. A: Chem. 356 (2012) 100–105.
- [62] S. Gerei, E. Rozhkova, Y.B. Gorokhovatsky, J. Catal. 28 (1973) 341–350.
- [63] T. Hoost, K. Laframboise, K. Otto, Appl. Catal. B: Environ. 7 (1995) 79–93.
- [64] P. Concepción, P. Botella, J.M.L. Nieto, Appl. Catal. A: Gen. 278 (2004) 45–56.
- [65] B. Wang, X. Wu, R. Ran, Z. Si, D. Weng, J. Mol. Catal. A: Chem. 361–362 (2012) 98–103.
- [66] V.R. Choudhary, S. Banerjee, S.G. Pataskar, Appl. Catal. A: Gen. 253 (2003) 65–74.
- [67] B. Solsona, T. Garcia, E. Aylon, A.M. Dejoz, I. Vazquez, S. Agouram, T.E. Davies, S.H. Taylor, J. Chem. Eng. 175 (2011) 271–278.
- [68] S. Swislocki, K. Stowe, W.F. Maier, J. Catal. 316 (2014) 219–230.
- [69] L.G. Chen, Y.L. Zhu, H.Y. Zheng, C.H. Zhang, Y.W. Li, Appl. Catal. A: Gen. 411 (2012) 95–104.
- [70] W. Rachmady, M.A. Vannice, J. Catal. 208 (2002) 170–179.